Sound velocities, and mechanical and electronic properties of the intermetallic compound $CeAl_2$ at high pressure

Yaoshi Cheng,[1] Ruiqi He,[1] Yuanhua Xia,[1] Tiexin Han,[1] Leiming Fang,[1,*] Shiliang Huang,[2] and Benqiong Liu[1,†]

[1]*Key Laboratory of Neutron Physics, and Institute of Nuclear Physics and Chemistry, China Academy of Engineering Physics (CAEP), Mianyang 621999, People Republic of China*

[2]*Institute of Chemical Materials, China Academy of Engineering Physics (CAEP), Mianyang 621999, People Republic of China*

(Received 19 December 2021; revised 31 January 2022; accepted 10 February 2022; published 18 February 2022)

Compressional (V_P) and shear (V_S) wave velocities of polycrystalline $CeAl_2$ have been measured up to 12.5 GPa at room temperature by ultrasonic interferometry in a multi-anvil apparatus. Both V_P and V_S show a weak pressure dependence up to 7.5 GPa, and then a remarkable discontinuity is observed which supports the earlier report about a volume collapse in this material. An anomaly has also been found in the pressure derivative of resistance dR/dP at around $P = 7.5$ GPa. Based on the experimental data, the high-pressure behaviors of the bulk and shear moduli are investigated. Complementary to the measured data, the single-crystal elastic constants are computed by first-principles calculations. Both the pressure-dependent C_{11} and C_{44} exhibit a change of slope at about $P = 7.5$ GPa. At low pressure, the observed flat curve for the shear modulus may be due to C_{44} which shows negligible pressure dependence. At higher pressure, C_{44} softens more rapidly and the mechanical instability occurs at $P > 15$ GPa. The calculated electronic densities of states show that sharp peaks near the Fermi level are mainly originated from the $4f$ and d states, which may be responsible for the Ce-Ce covalent bond. High pressure leads to a broadening of $4f$ band and an increase of the d/f hybridization.

DOI: 10.1103/PhysRevB.105.064106

I. INTRODUCTION

$CeAl_2$ belongs to the REAl$_2$ (RE=rare-earth) series of intermetallic compounds, which crystallizes in the $MgCu_2$-type C15 Laves phase structure (space group $Fd\bar{3}m$, No. 227). It is a well-known prototype material for the study of the interplay between Kondo spin compensation effect and the RKKY interaction, and has been extensively studied both experimentally and theoretically [1–4]. For examples, the unusual magnetic excitation spectrum of $CeAl_2$ with a two-peak structure [5] cannot be described by the conventional crystal field (CF) model, since one would expect for the Ce^{3+} ions a CF splitting into a Γ_7 and a Γ_8 state with single transition. To explain the additional inelastic peak, a simplified dispersionless model was proposed by Thalmeier and Fulde [6] implying that a vibronic bound state (VBS) between a CF excitation and phonons was formed. The original VBS model employed in the cubic system has been then generalized to tetragonal systems because similar unusual excitations have also been observed in other Ce-based compounds like $CePd_2Al_2$ [7], $CeCuAl_3$ [8], and most recently in $CeAuAl_3$ [9,10].

Besides, the complicated nature of the magnetism of $CeAl_2$ is puzzling and has been investigated for many years. At low temperature ($T = 3.8$ K), $CeAl_2$ was reported to order in an incommensurate antiferromagnetic structure with the propagation wave vector $\mathbf{k}_{IC} = (\frac{1}{2} + \delta, \frac{1}{2} - \delta, \frac{1}{2})$ [11] with $\delta = 0.112$. By single-crystal neutron diffraction, Shapiro *et al.* [12] observed additional weaker superlattice peaks at $\mathbf{k}_C = (\frac{1}{2}, \frac{1}{2}, \frac{1}{2})$, and showed first definitive evidence for a multiple-q magnetic structure. Later, Forgan *et al.* [13] conducted neutron diffraction measurements in an applied magnetic field and showed that $CeAl_2$ is double-q and the magnetic structure is nonchiral spiral. The fascinating magnetic behavior in this system was assumed to be associated with the strong hybridization between the $4f$ electrons and the conduction electrons [11].

Since the unstable $4f$ electrons and the magnitude of hybridization are sensitive to external pressure, the community has devoted great efforts to understanding various properties of $CeAl_2$ under high pressure. For instances, electrical resistivity as well as the magnetoresistance has been extensively investigated under high pressure [14–19]. An anomalous Hall effect of single crystal $CeAl_2$ has been observed and the sign of Hall coefficient R_H changes at 2.7 GPa where a quantum critical point may exist [15], indicating the crossover in the electronic state from $4f$-localized to itinerant state [20]. Low-temperature specific heat of $CeAl_2$ under pressure was measured to obtain the $P - T$ phase diagram and interpret the discrepancy between results of magnetic and thermodynamic measurements [21,22]. High pressure effects on $CeAl_2$ and $CeCuAl_3$ by NMR have been reported [23].

Especially, there have been a number of contradictory experimental results of the compressibility. At first, Croft and Jayaraman [24,25] reported a pressure-induced valence transition at about 6.5 GPa, where a volume collapse ($V/V_0 \approx 0.93$, or around 7% compression) was observed without any change of crystal structure. Bartholin *et al.* [26] performed both neutron and x-ray diffraction experiments under high

*flmyaya2008@163.com
†liubenqiong@caep.cn

pressure, and showed agreement with previous results, i.e., they detected a drop in the lattice parameter of $CeAl_2$ due to a change of Ce ion from Ce^{3+} to Ce^{4+} at around 7 GPa with a relative volume change of about 3.8%. As the thermopower proved effective to detect valence transitions in metallic systems [27], Vijayakumar *et al.* [28] carried out high-pressure thermopower measurements of $CeAl_2$ and found a maximum at about 8 GPa which could be attributed to continuous valence transitions of Ce ions. Ramesh and Holzapfel's paper [29] also supported that there was a clear discontinuous volume collapse near 7.7 GPa, with a volume change of only 1%. They suggested that the isostructure phase transition in $CeAl_2$ resembles the $\gamma - \alpha$ transition in pure Ce metal, which is believed to result from the delocalization of the $4f$ shell [18]. However, Barbara *et al.* [30,31] did high-pressure x-ray diffraction up to 15 GPa and observed no well defined transition. Similarly, Vedel *et al.* [32,33] measured the compression curve of $CeAl_2$ and revealed no detectable volume discontinuity under pressures up to 20 GPa. More than one decade later, Chandra Shekar *et al.* [34] reinvestigated this issue by high-pressure x-ray diffraction experiments up to ≈23 GPa and showed pronounced anomalous compressibility behavior of $CeAl_2$ between 2 and 6 GPa. Recently, Tateno *et al.* [35] also found no discontinuous change in the compression curve below 20 GPa, and they observed that a full width at half maximum was enhanced above 20 GPa for several Bragg peaks suggesting a new pressure-induced structural phase transition from cubic to tetragonal structure.

The large discrepancies on the possible phase transition might be associated with very tiny structure distortions and the sensitivity to different probing techniques and hydrostatic conditions. Acoustic velocity measurement is of high sensitivity to study phase transitions. In order to address the long debate on the compression curves of $CeAl_2$, in this paper we have reinvestigated this matter by comprehensively studying the ultrasonic velocities, mechanical and electronic properties under high pressure. Our results show clear anomaly/discontinuity at $P = 7.5$ GPa, suggesting that a valence transition in $CeAl_2$ might occur. Other possible causes may be related to the softening of the transverse acoustic (TA) phonon branches of which the slopes are determined by the elastic constant C_{44}, or the delocalization of $4f$ electron of the Ce^{3+} ions.

II. METHODS

The polycrystalline sample of intermetallic compound $CeAl_2$ was prepared by *arc* melting of pure Ce (99.9%, Alfa Aesar) and Al (99.99%, Alfa Aesar) in argon gas atmosphere, and an excess rare earth (Ce:Al = 1.05:2) was added to compensate for their loss during melting. The phase purity was confirmed by x-ray diffraction measurements, as shown in Fig. 1. The powder x-ray diffraction pattern was collected on Bruker D8 X-ray diffractometer equipped with Cu Kα radiation source ($\lambda = 1.5418$ Å, 40 kV, 40 mA). In order to perform the ultrasonic experiments, the sample was processed into a disk of 2 mm in length and 2.5 mm in diameter by wire cutting method. Both parallel faces of the disk were polished flat by diamond lapping films so as to ensure good ultrasonic signals.

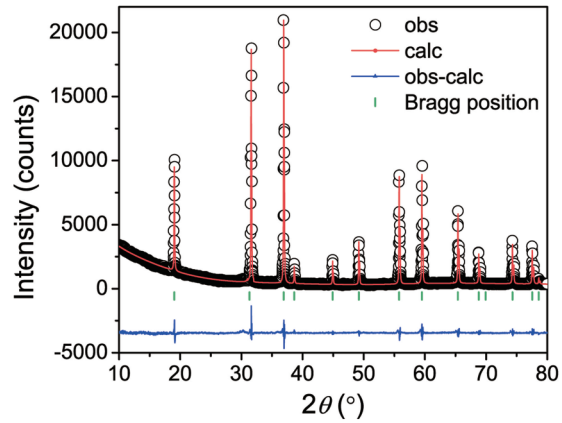

FIG. 1. X-ray diffraction pattern of $CeAl_2$ at room temperature.

The polished sample is 0.166 g, with 0.679 mm in length. The bulk density of the sample was measured by Archimedes' immersion method, $\rho = 4.987$ g/cm^3, about 101.3% of calculated density based on the lattice parameter $a = 8.062$ Å.

The high-pressure *in situ* ultrasonic interferometric measurement is based on 14/8 cell assembly as shown in Fig. 2 at room temperature. The high pressure is achieved with the 6×14MN hinge-type double-stage cubic large-volume press, which is installed in the High Pressure Laboratory at China Mianyang Research Reactor (CMRR) neutron scattering facility. A dual mode $LiNbO_3$ disk, which excites the acoustic signals (10° rotated Y-cut) as a transducer (the resonance frequencies for compressional and shear waves are 50 and 30 MHz, respectively), meanwhile serving as a receiver, is mounted on the back corner of one of the eight WC cubes. The WC anvil serves as an acoustic buffer cube to transmit the high-frequency signals (20 to 70 MHz) into the sample. The MgO octahedron and a pyrophyllite tube are used as pressure transmission mediums. A double-side polished polycrystalline Al_2O_3 buffer rod with density $\rho = 3.914(2)$ g/cm^3 is employed to transmit acoustic signals. There is a 2μm-thick gold foil inserted between the buffer rod and the sample to enhance their acoustic coupling. The back of sample is connected with a NaCl cylinder and a ceramic rod, in order to provide a quasihydrostatic pressure environment for $CeAl_2$ sample.

Figure 3 is a schematic diagram showing the principle of travel time measurements using interferometric method. The acoustic signals are transmitted via the WC anvil, buffer rod, and the sample. The $LiNbO_3$ disk receives the echoes from the interfaces perpendicular to the wave propagation path, and converts acoustic signals to electrical signals. Time differences Δt between the pulses are corresponding to the waves traveling round trip in the buffer rod and sample. To obtain the travel times, we use the transfer function method of Li *et al.* [36] to acquire acoustic responses in the frequency range of 25–70 MHz with a pulse echo overlap (PEO) analysis at monochromatic frequencies. The uncertainties are estimated to be less than 0.2% in elastic wave velocities and less than 2% in the derived elastic moduli.

First-principles calculations were performed using the Vienna *ab initio* simulation package (VASP) [37,38], with the projector-augmented wave (PAW) scheme. The exchange and

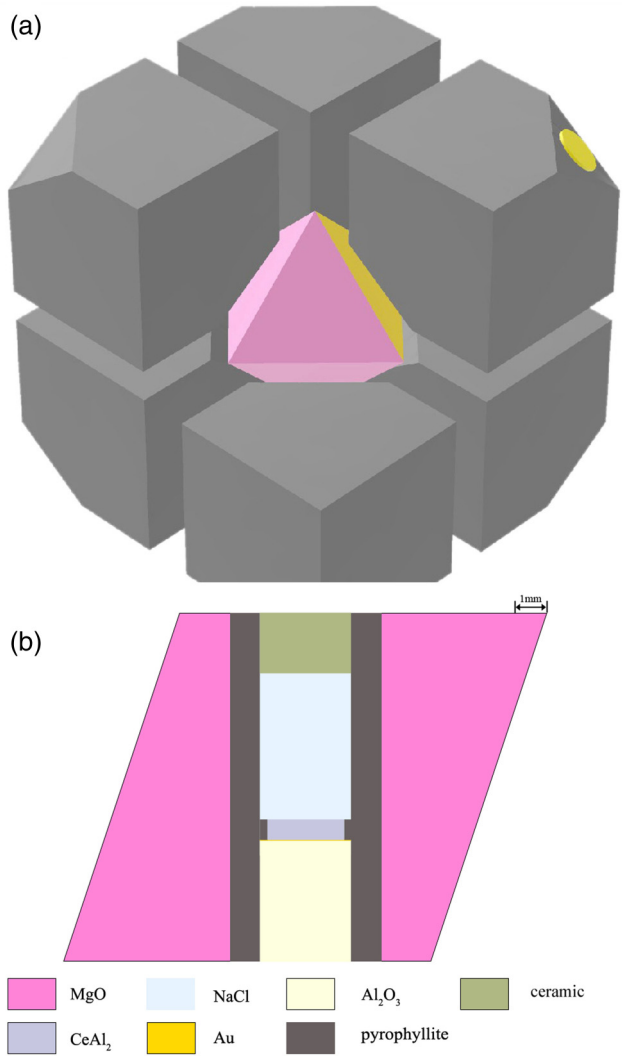

FIG. 2. (a) Schematic diagram of the second-stage WC-anvils and cell assembly for high-pressure ultrasonic measurements at room temperature in large-volume press. (b) Cross section of the 14/8 cell assembly.

correlation energies were taken in the generalized-gradient approximation (GGA) according to Perdew-Burke-Ernzerhof prescription. The plane-wave cutoff energy was tested and set to 500 eV. According to Monkhorst-Pack scheme, the k-point meshes in the Brillouin zone were sampled by $11\times11\times11$ grids. Other parameters include a convergence criterion of the total energy of 10^{-8} eV, and the Hellmann-Feynman force of 0.01 eV/Å.

III. RESULTS AND DISCUSSION

A. Velocities and elastic moduli

The specimen length at high pressure can be obtained from the observed travel times of P and S waves by the Cook's method [39]

$$\frac{L_0}{L} = 1 + \frac{1+\alpha\gamma T}{3\rho_0 L_0^2}\int \frac{dP}{\frac{1}{t_P^2} - \frac{4}{3t_S^2}}, \tag{1}$$

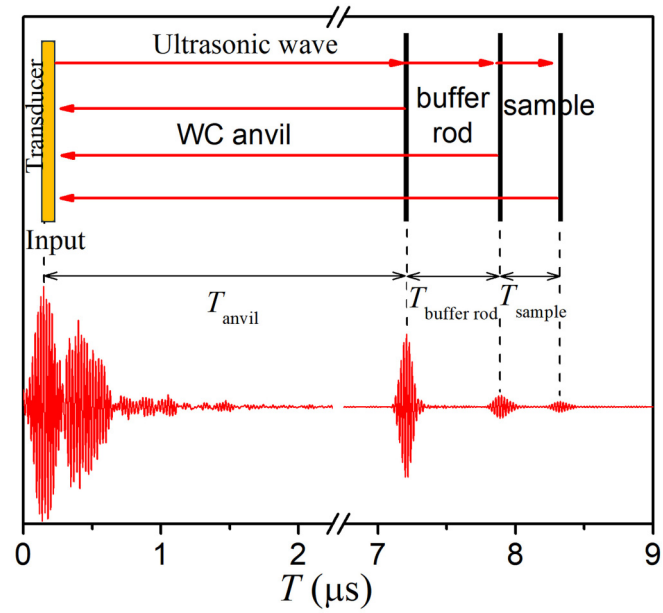

FIG. 3. Compressional wave signal (50 MHz) observed at 8.75 GPa, showing the reflections from the anvil, the Al_2O_3 buffer, and the $CeAl_2$ sample, respectively.

where t_P and t_S represent compressional and shear wave travel times in specimen length L, respectively. ρ_0 and L_0 denote the density and the length of the sample at ambient condition, respectively. α is the thermal expansion coefficient, γ is the Grüneisen parameter, and T represents temperature. At room temperature, the term $\alpha\gamma T$ is around 0.01 for most materials [40]. The densities and unit-cell volumes of $CeAl_2$ sample can be obtained from the change of length,

$$\frac{\rho_0}{\rho} = \frac{V}{V_0} = \left(\frac{L}{L_0}\right)^3. \tag{2}$$

The bulk B, shear G, and elastic longitudinal L_M moduli under high pressure can be obtained from the velocity and density data [41]:

$$B = \rho V_P^2 - \frac{4}{3}\rho V_S^2, \tag{3}$$

$$G = \rho V_S^2, \tag{4}$$

$$L_M = \rho V_P^2 = B + \frac{4}{3}G, \tag{5}$$

where V_P and V_S are velocities of the compressional and shear waves ($V_{(P,S)} = \frac{2L}{t_{(P,S)}}$), respectively. All experimental data obtained from measured travel times are listed in Table I.

By fitting the velocity and density data to the third-order Eulerian finite strain equations [42], one can obtain the adiabatic bulk B_0 and shear G_0 moduli as well as their pressure derivatives at ambient conditions,

$$\rho V_P^2 = (1-2\epsilon)^{\frac{5}{2}}(L_1 + L_2\epsilon), \tag{6}$$

$$\rho V_S^2 = (1-2\epsilon)^{\frac{5}{2}}(M_1 + M_2\epsilon), \tag{7}$$

TABLE I. Experimental data for $CeAl_2$ under pressure at room temperature.

P (GPa)	$2t_P$ (μs)	$2t_S$ (μs)	L (mm)	ρ (g/cm^3)	V_P (km/s)	V_S (km/s)	B (GPa)	G (GPa)	L_M (GPa)
2.5	0.2446	0.4366	0.6727	5.129	5.50	3.08	90.23	48.70	155.17
3.75	0.2414	0.4324	0.6700	5.195	5.55	3.09	93.49	49.86	159.98
5	0.2394	0.4300	0.6671	5.259	5.57	3.10	95.83	50.63	163.34
6.25	0.2388	0.4296	0.6643	5.326	5.56	3.09	96.93	50.94	164.85
7.5	0.2414	0.4308	0.6608	5.410	5.47	3.07	94.27	50.92	162.16
8.75	0.2624	0.4366	0.6513	5.651	4.96	2.98	72.19	50.30	139.25
10	0.2606	0.4448	0.6492	5.708	4.98	2.92	76.81	48.62	141.63
11.25	0.2546	0.4564	0.6493	5.701	5.10	2.85	86.80	46.17	148.35
12.5	0.2522	0.5044	0.6506	5.669	5.16	2.58	100.60	37.73	150.91

where the strain $\epsilon = \frac{1}{2}[1 - (\frac{V_0}{V})^{2/3}]$, and L_1, L_2, M_1, M_2 are fitted coefficients,

$$L_1 = B_0 + \frac{4G_0}{3}, \tag{8}$$

$$L_2 = 5L_1 - 3B_0\left(B_0' + \frac{4G_0'}{3}\right), \tag{9}$$

$$M_1 = G_0, \tag{10}$$

$$M_2 = 5G_0 - 3B_0G_0'. \tag{11}$$

A least-squares fitting yields $B_0 = 82.56$ GPa, $B_0' = 2.85$, $G_0 = 48.05$ GPa, and $G_0' = 0.59$.

Figure 4 shows the experimentally measured wave velocities and the derived elastic moduli of polycrystalline $CeAl_2$ under high pressure up to 12.5 GPa at room temperature. One can see that both compressional and shear wave velocities exhibit negligible pressure derivative at low pressures up to 7.5 GPa. Anomalous behavior can be readily observed as pressure increases, at first there appears a sudden drop for V_P and followed by an increase with pressure. Linear least-squares fittings show that the pressure dependence is $\partial V_P/\partial P \approx 0.056$ km/s GPa^{-1} for $P > 7.5$ GPa. In the case of V_S, it exhibits a discernible slope change at around 7.5 GPa and then it begins to decrease more rapidly with the a negative slope $\partial V_S/\partial P = -0.089$ km/s GPa^{-1}. Similar distinct anomaly can be observed in the bulk and shear moduli as shown in Fig. 4(b). At 7.5 GPa, the bulk modulus shows a softening and followed by a recovery stiffening. Such softening might be caused by the $4f$ electron delocalization, as the Ce-Ce interatomic spacing (3.47 Å at ambient pressure) becomes close to the critical distance ≈3.3 Å for a localized to itinerant transition [18,43,44]. At 7.5 GPa, the Ce-Ce distance is calculated as $d = 3.34$ Å. From Eqs. (1) and (2), the relative volume V/V_0 can be obtained and shows a collapse at $P = 7.5$ GPa, which may be due to valence transition in $CeAl_2$ as originally proposed by Croft and Jayaraman [24,25].

B. Electrical resistance

We have also measured the electrical resistance (Fig. 5) up to a maximum pressure of 15 GPa by using a hinge-type cubic large-volume press. The four-probe method is utilised to record data. A piece of $CeAl_2$ sample (about 1 mm×1 mm×3 mm) cut from the same ingot used for ultrasonic measurements is mounted in a MgO octahedron. Two sheets of copper are pressed against the sample.

In Fig. 5, one can find a clearly visible anomaly in the derivative of the resistance $\frac{dR}{dP}$ at around $P = 7.5$ GPa, showing a striking similarity to the ultrasonic experimental results. Probst and Witig [18] have suggested that $CeAl_2$ undergoes an electronic transition analogous to the $\gamma - \alpha$ transition in Ce metal in the pressure range 5–10 GPa. But Barbara *et al.* [30] concluded that hydrostatic pressure cannot produce such a transition but a simple crossover from weak to strong Kondo behavior. In a recent paper [19], the authors have measured the pressure dependence of the electrical resistivity at different

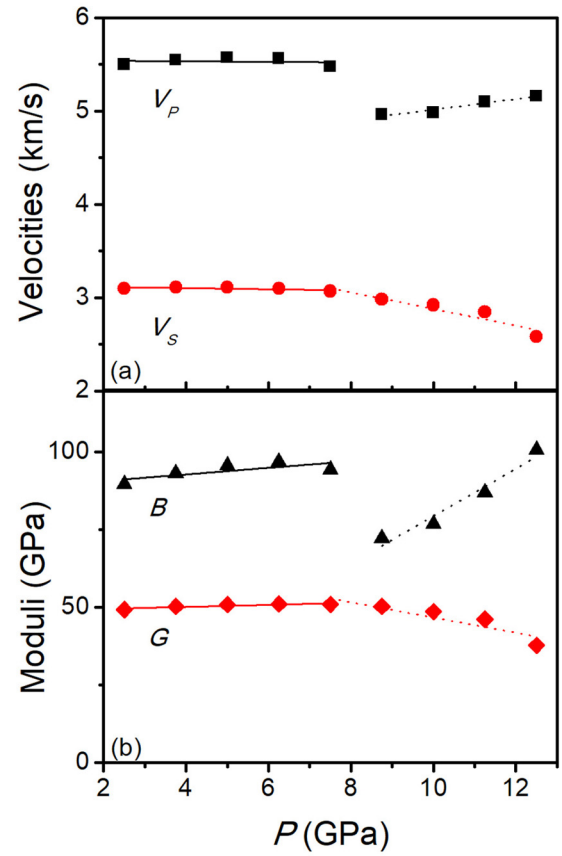

FIG. 4. (a) Elastic wave velocities (V_P and V_S), (b) bulk and shear moduli (B and G) of the polycrystalline $CeAl_2$ at high pressure.

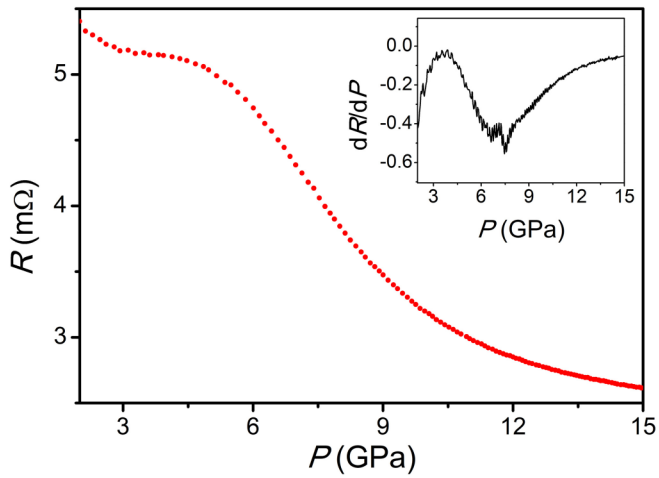

FIG. 5. The electrical resistance of $CeAl_2$ as a function of pressure. The inset shows the pressure derivative of resistance for $CeAl_2$.

temperatures. They found that the resistivity increased with pressure followed by a maximum at P_{max}. P_{max} increases with temperature, and at room temperature P_{max} seems to shift to ≈6 GPa. These maximum humps are also interpreted as the crossover in the electronic state of $CeAl_2$.

C. Elastic constants

In order to understand the anomalous behavior of the elastic properties, we have calculated the elastic constants of single crystal $CeAl_2$. There are 24 atoms in the conventional unit cell of $CeAl_2$. The lattice parameter $a_0 = 8.04$ Å [45]. For the geometry optimization, we start with the experimental data and calculate the volume (V) dependence of the total energy (E). By a least-squares fit of the $E - V$ curve to the third-order Birch-Murnaghan equation of state (EOS) [46], the lattice parameter a_0, equilibrium volume V_0, the bulk modulus B_0 as well as its pressure derivative B_0' can be obtained, as listed in Table II compared with previous theoretical and experimental results. Our value for the lattice parameter $a_0 = 7.945$ Å is in good agreement with the theoretical work $a_0 = 7.941$ Å [3], but lower than the experimental values [32,35,45,47], which can be expected since DFT calculations are set to 0 K and we have neglected the thermal expansion. Using a thermal expansion coefficient for $CeAl_2$ of $\alpha_{(30-670^\circ C)} = 12.11\times10^{-6}\,^\circ C^{-1}$ [48], one can roughly estimate the volume at room temperature in slightly better agreement with experiments. However, it should be noted that $\alpha(T)$ behaves anomalously in many rare earth intermetallics, particularly at low temperatures. Another possible reason is that our calculation is nonspin polarized, whereas $CeAl_2$ orders antiferromagnetically below $T_N = 3.8$ K. The calculated bulk modulus and its first derivative, as obtained from the $E - V$ fit are $B_0 = 73.0$ GPa and $B_0' = 3.69$, are well within the range of reported values, respectively.

Figure 6 shows the volume compression V/V_0 of $CeAl_2$ as a function of pressure. For comparison, data from earlier studies are also included. It can be seen from Fig. 6(a) that both calculated and previous experimental results show very good agreements at low pressure ($P < 10$ GPa). As pressure increases, the calculated value of V/V_0 decreases slightly more slowly than the experimental curves. In Fig. 6(b), it is apparent that the relative volume obtained from our ultrasonic measurements shows a pronounced discontinuity starting at around $P = 7.5$ GPa, supporting the previously observed anomalous compressibility [24–26,29]. The third-order Birch-Murnaghan EOS, fitted to the experimental $P - V$ data below 7.5 GPa gives bulk modulus and its derivative as $B_0 = 85.26 \pm 1.56$ GPa, and $B_0' = 3.32 \pm 0.62$, respectively.

For cubic systems, there are three independent elastic constants C_{11}, C_{12}, and C_{44}, which can be obtained by using the "stress-strain technique" based on applied small deformations [50–52]. The calculated elastic constants at ambient pressure and high pressure up to 15 GPa are summarized in Table III, compared with experimental results at zero pressure. The calculated results at zero pressure, $C_{12} = 29.5$ GPa and $C_{44} = 42.4$ GPa are in good agreement with those from ultrasonic measurements ($C_{12} = 29.8$ GPa, $C_{44} = 43.8$ GPa). However, our $C_{11} = 166.4$ GPa is ≈13% higher compared to the experimental value $C_{11} = 147.2$ GPa reported by Penney *et al.* [45]. In Fig. 7, the elastic constants C_{11}, C_{12}, C_{44}, and the elastic shear modulus $C' = \frac{C_{11}-C_{12}}{2}$ are plotted as a function of pressure. The elastic anisotropy of cubic systems can be written as $A = \frac{2C_{44}}{C_{11}-C_{12}}$. For a complete isotropic

TABLE II. Optimized lattice parameter a_0, the equilibrium volume V_0, Ce-Ce distance d, and bulk modulus B_0 and its pressure derivative B_0' of $CeAl_2$.

	a_0 (Å)	V_0(Å^3)	d (Å)	B_0	B_0'	Remarks
This paper	7.9449	501.5	3.47	73.0	3.69	DFT, $P = 0$ GPa
	7.7194	460.0	3.34			DFT, $P = 7.5$ GPa
	7.5535	431.0	3.27			DFT, $P = 15$ GPa
	8.062	523.96				XRD
Ding *et al.* [3]	7.941	500.8		64.2		DFT
Vedel *et al.* [32]				66.4 ±3	3.3 ±0.4	
Chandra Shekar *et al.* [34]	8.054 ±0.002	522.4		234 ±45	−3.7 ±9.3	XRD
Tateno *et al.* [35]	8.055 ± 0.002	522.6		62	3.0	XRD
Penney *et al.* [45]	8.04	519.7		68.7 ±2	3.0 ±1	XRD
				68.9 ±1.5		ultrasonic
Raghavan *et al.* [47]	8.06	523.6		66.4		
Rossignol [49]				75.4		neutron

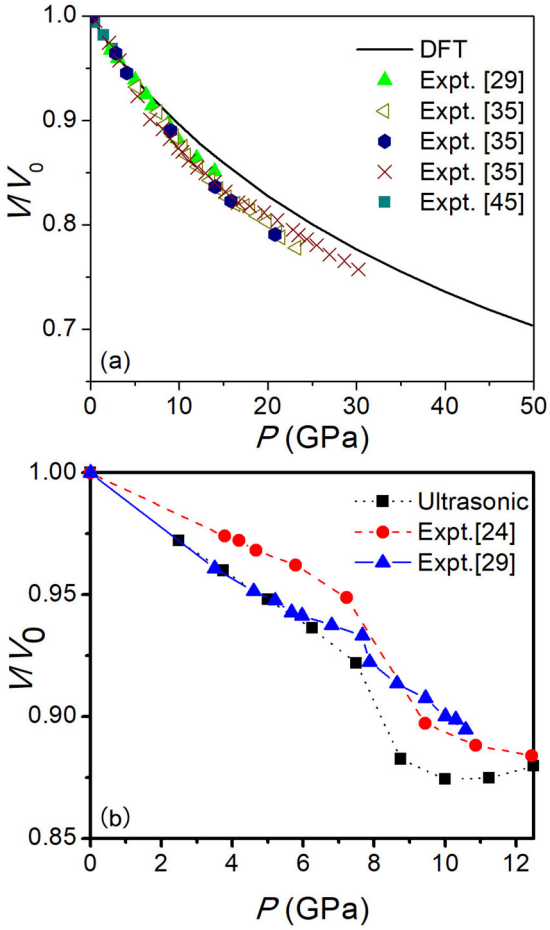

FIG. 6. Volume change of $CeAl_2$ as a function of pressure. (a) DFT calculated results and (b) data derived by ultrasonic measurements, compared with previous experimental results.

material, $C' = C_{44}$ and $A = 1$. As pressure increases, $CeAl_2$ exhibits strong anisotropy, which is due to a rapid decrease in the trigonal shear modulus C_{44} and an increase in the tetragonal shear modulus C'. One can find that the elastic constant C_{12} increases almost linearly with pressure, and $CeAl_2$ is mechanically stable throughout the pressure range up to 15 GPa.

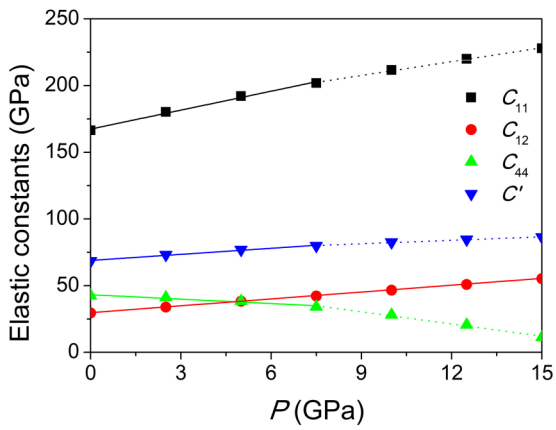

FIG. 7. Calculated elastic constants C_{11}, C_{12}, C_{44}, and the elastic shear modulus C' of $CeAl_2$. The dashed line denotes a different slope by linear least-squares fitting from the solid line.

TABLE III. The calculated independent elastic constants (in GPa) C_{11}, C_{12}, C_{44}, C' and the elastic anisotropy $A = \frac{2C_{44}}{C_{11}-C_{12}}$ of $CeAl_2$ under pressure.

P	C_{11}	C_{12}	C_{44}	C'	A
0.0 Expt.[a]	147.2	29.8	43.8	58.7	0.75
0.0 Expt.[b]	147.3	30.5	44.0	58.4	0.75
0.0 Expt.[c]	145.2	29.2	43.4	58.0	0.75
0.0 DFT [d]	134.0	27.1	45.8	53.45	0.86
0.0	166.4	29.5	42.4	68.45	0.62
2.5	180.2	33.9	41.2	73.14	0.56
5.0	192.1	38.2	38.4	76.92	0.50
7.5	201.9	42.2	34.2	79.86	0.43
10.0	211.6	46.6	28.1	82.52	0.34
12.5	220.0	50.8	20.6	84.61	0.24
15.0	228.0	55.2	11.3	86.38	0.13

[a]Data obtained from the sample grown in Yorktown (Y1) in Ref. [45].
[b]Data obtained from the sample grown in Yorktown (Y2) in Ref. [45].
[c]Data obtained from the sample grown in Grenoble (G) in Ref. [45].
[d]Reference [3].

For C_{11} and C_{44}, the situations are different. C_{11} increases monotonically with pressure with a slope of $k = 4.73$ at low pressures $P \leqslant 7.5$ GPa, and from then on it increases more slowly and the slope changes to $k = 3.47$. For C_{44}, at first it is larger than C_{12} at low pressures ($P \leqslant 5$ GPa), decreasing very slowly with a slope of $k = -1.10$ till $P = 7.5$ GPa and then falling more rapidly with increasing pressure ($k = -3.05$). The slope changes of both C_{11} and C_{44} appear at around $P = 7.5$ GPa, where by coincidence the anomalies in V_P and V_S from our ultrasonic measurements occur. Although the current theoretical results cannot completely cover all the remarkable experimental features, they show some similarities to some extent. The weak pressure effect of C_{44} at low pressures ($P \leqslant 7.5$ GPa) may be responsible for the experimentally observed slow increase in the shear wave velocity and hence the shear modulus [53].

The elastic instability occurs ($C_{44} < 0$) above 15 GPa, as the Born's mechanical stability criteria [54] has been violated,

$$C_{11} + 2C_{12} > 0, C_{44} > 0, C_{11} - C_{12} > 0, \qquad (12)$$

implying that the system is no longer stable against the shear given by one of the transverse acoustic phonon modes. As reported in Ref. [55], large phonon softening (reduction in the phonon frequency ω) was observed in both the Δ_5 and Σ_3 TA branches, for which the slopes were determined by C_{44}. In Table IV, long-wavelength acoustic modes generated by shear distortions of the cubic crystal structure representing solutions of the dynamical matrix for different wave vectors $\mathbf{k}$ are tabulated. One can find that if $C_{44} < 0$, the crystal is unstable against the transverse acoustic mode with $\mathbf{k} = [\zeta, 0, 0]$ and polarization vector along [010] or [001], as well as $\mathbf{k} = [0, \zeta, \zeta]$ and polarization vector along [100] as observed in Ref. [55]. We predict that by inelastic neutron scattering measurements one might also observe TA phonon softening along the high symmetry directions X $\rightarrow$ L ($\mathbf{k} = [0, \zeta, 0]$) and W $\rightarrow$ K ($\mathbf{k} = [-\zeta, \zeta, 0]$), where the high symmetry points X $= (\frac{1}{2}, 0, \frac{1}{2})$, L $= (\frac{1}{2}, \frac{1}{2}, \frac{1}{2})$, W $= (\frac{1}{2}, \frac{1}{4}, \frac{3}{4})$, and K $= (\frac{3}{8}, \frac{3}{8}, \frac{3}{4})$.

TABLE IV. For the acoustic modes, the solutions of the dynamic matrix for selected wave vectors $\mathbf{k} = [\zeta, 0, 0]$, $[0, \zeta, 0]$, $[-\zeta, \zeta, 0]$, and $[0, \zeta, \zeta]$ are listed, where the subscripts denote the directions of motion of the atoms.

$\mathbf{k} = [\zeta, 0, 0]$	$\mathbf{k} = [0, \zeta, 0]$	$\mathbf{k} = [-\zeta, \zeta, 0]$	$\mathbf{k} = [0, \zeta, \zeta]$
$\rho\omega^2_{[100]} = C_{11}\zeta^2$	$\rho\omega^2_{[010]} = C_{11}\zeta^2$	$\rho\omega^2_{[110]} = (C_{11} - C_{12})\zeta^2$	$\rho\omega^2_{[0\bar{1}1]} = (C_{11} - C_{12})\zeta^2$
$\rho\omega^2_{[010]} = C_{44}\zeta^2$	$\rho\omega^2_{[001]} = C_{44}\zeta^2$	$\rho\omega^2_{[001]} = 2C_{44}\zeta^2$	$\rho\omega^2_{[100]} = 2C_{44}\zeta^2$
$\rho\omega^2_{[001]} = C_{44}\zeta^2$	$\rho\omega^2_{[100]} = C_{44}\zeta^2$	$\rho\omega^2_{[\bar{1}10]} = (C_{11} + C_{12} + 2C_{44})\zeta^2$	$\rho\omega^2_{[011]} = (C_{11} + C_{12} + 2C_{44})\zeta^2$

Previously, Godet and Purwins [56] measured the elastic constants of $CeAl_2$ at low temperature and observed a softening of the elastic constants C_{44} of 30% with decreasing temperature which can be due to a magnetoelastic coupling. Besides, Roth *et al.* [57] studied the C_{44} mode in high magnetic fields up to 7 Tesla. They argued the interpretation in terms of magnetoelastic interaction [58] and demonstrated that the magnetic effect should be most possibly responsible for the softening of C_{44}. Another potential reason might be the interaction between the conduction band and $4f^1$ electron, which plays an important role in understanding the low temperature physics of Ce-based compounds. Here, we find that the elastic constant C_{44} is also pressure dependent, and the observed anomalous behavior of elastic wave velocities and elastic moduli in terms of slope change and discontinuities under pressure might be associated with softening of the TA phonon modes.

Based on the single-crystal elastic constants of $CeAl_2$, one can further evaluate the polycrystalline average isotropic bulk modulus B and shear modulus G by using the Voigt-Reuss-Hill method [59],

$$B_R = B_V = (C_{11} + 2C_{12})/3, \tag{13}$$

$$G_V = (C_{11} - C_{12} + 3C_{44})/5, \tag{14}$$

$$G_R = 5(C_{11} - C_{12})C_{44}/[4C_{44} + 3(C_{11} - C_{12})], \tag{15}$$

$$B = \frac{B_R + B_V}{2}, \tag{16}$$

$$G = \frac{G_R + G_V}{2}. \tag{17}$$

TABLE V. The calculated bulk B, shear G, and Young's moduli Y (in GPa), Poisson ratio ν of $CeAl_2$ under pressure.

P	B	G	Y	ν
0.0 Expt.[a]	68.9	49.26	119.33	0.168
0.0 DFT[b]	62.7	48.85	116.34	0.191
0.0	75.16	51.44	125.65	0.221
2.5	82.71	51.94	128.85	0.240
5.0	89.52	50.90	128.38	0.261
7.5	95.44	48.40	124.19	0.283
10.0	101.62	43.99	115.32	0.311
12.5	107.21	37.88	101.67	0.342
15.0	112.82	29.32	80.95	0.380

[a]Data obtained from the sample grown in Yorktown (Y1) in Ref. [45].
[b]Reference [3].

The Young's modulus Y and Poisson's ratio ν can be given by

$$Y = \frac{9BG}{3B + G}, \tag{18}$$

$$\nu = \frac{3B - 2G}{2(3B + G)}. \tag{19}$$

The calculated bulk, shear, Young's moduli and Poisson's ratio for $CeAl_2$ are summarized in Table V. We note that the calculated bulk modulus B increases almost linearly, which cannot reproduce the break (a sudden decrease and followed by a stiffening recovery) as observed experimentally. The shear modulus G behaves similarly with the experimental data as the pressure increases. Young's modulus is a measure of stiffness of a solid material. It shows an slight increase at the beginning and then falls rapidly at higher pressure. The Poisson's ratio varies from 0.22 to 0.38 monotonically. According to Pugh [60], a high (low) ratio of shear to bulk modulus G/B is associated with brittleness (ductility) of the material, and the critical value separating ductile and brittle property is about 0.57. The theoretical value of $CeAl_2$ at ambient pressure is 0.68, while the experimental value is 0.58 close to the critical value, indicating that $CeAl_2$ can be slightly brittle.

D. Electronic density of states

The basic physical and chemical properties like elastic constants of the material are largely determined by its electronic structure. With the aim of further understanding the mechanical property of $CeAl_2$ from a microscopic viewpoint, we have calculated and analyzed the electronic density of states under high pressure.

Figures 8 and 9 show the total and partial densities of states (DOS) of $CeAl_2$, respectively. For the total DOS shown in

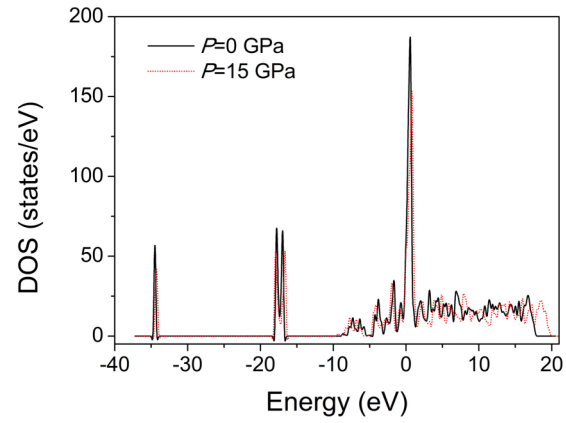

FIG. 8. Total densities of states of $CeAl_2$.

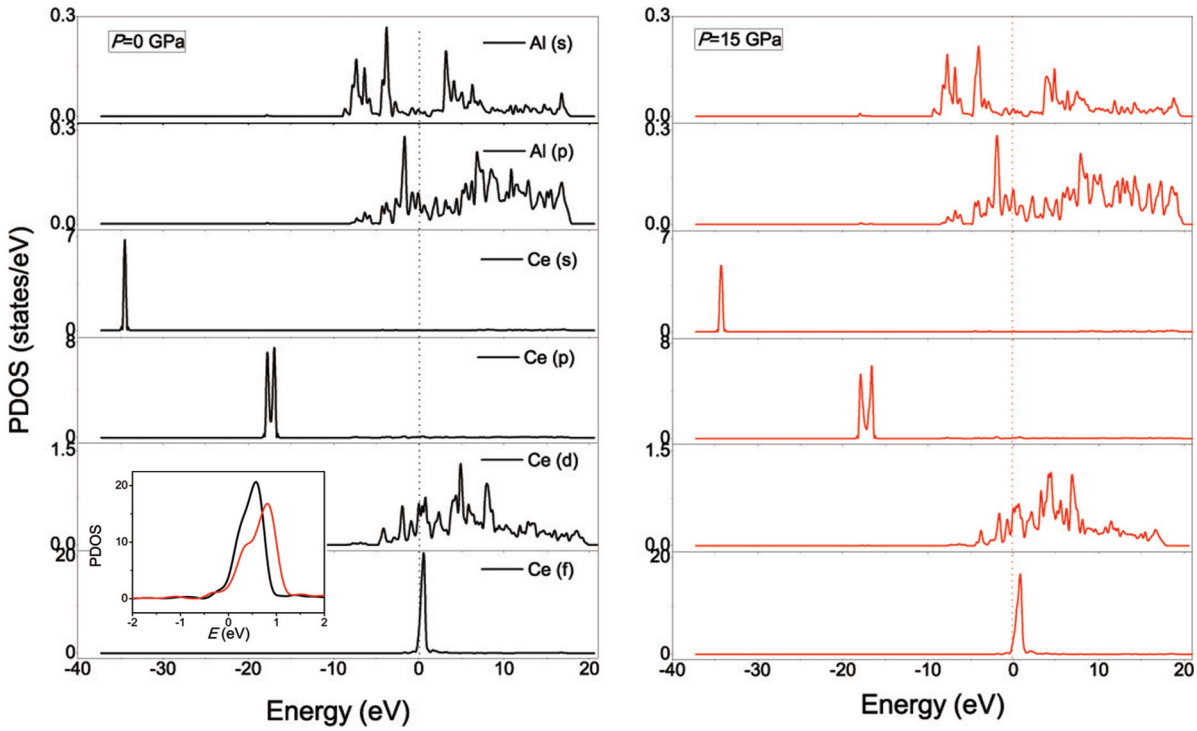

FIG. 9. Partial densities of states of $CeAl_2$. The inset shows the densities of states for Ce $4f$ band at $P = 0$ GPa (black) and $P = 15$ GPa (red).

Fig. 8, the most pronounced difference is the lowering of the peaks' height and the broadening of the peaks at high pressure $P = 15$ GPa. It is not surprising that as pressure increases, the Ce-Ce interatomic distance decreases ($d = 3.27$ Å at $P = 15$ GPa compared with $d = 3.47$ Å at ambient pressure), the overlap of the outer electronic shells of constituent atoms increases, which results in an increase in the band widths, the extent of spd/f hybridization.

One can find that the total DOS at the Fermi level mainly comes from the contribution of sharp $4f$ band and a small amount of Ce d states. There is a very narrow peak near –34 eV due to the flat bands of Ce s states. Between –18 and –16 eV, there exists a double-peak structure resulting from Ce p states. The spd/f hybridization is quite obvious. According to Ref. [61], the application of pressure can lead to the increase of the $4f$ electrons coupling with other band

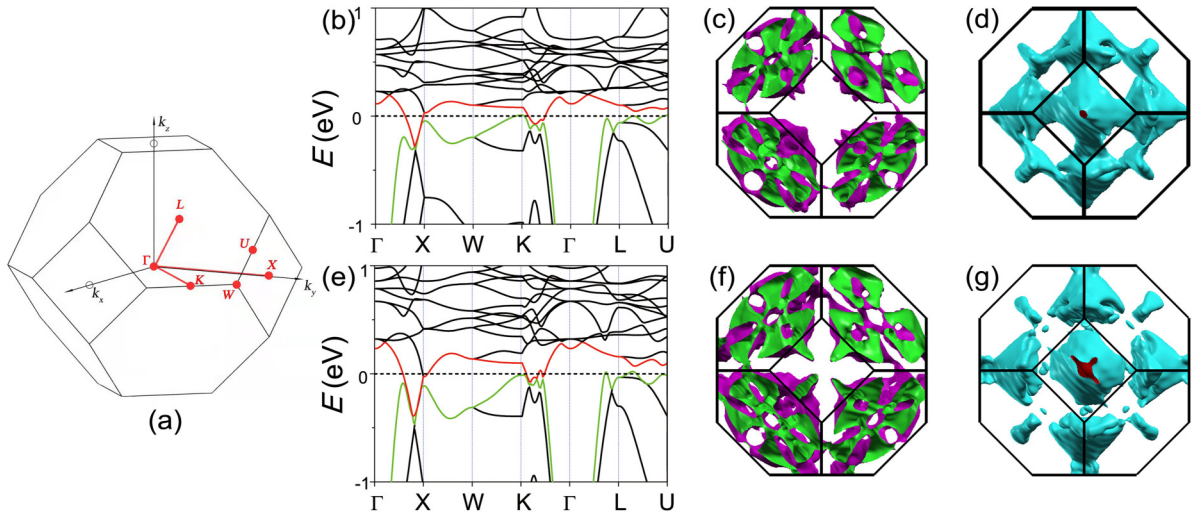

FIG. 10. The band structure and Fermi surfaces of $CeAl_2$. (a) The Brillouin zone with high-symmetry points for the $CeAl_2$ structure. (b) Band structure at $P = 0$ GPa. (c) Fermi surface sheets originating from the lower green band (the outer sheet) and (d) the higher red band (the inner sheet) at $P = 0$ GPa. (e) Band structure at $P = 15$ GPa. (f) Fermi surface sheets originating from the lower green band (the outer sheet) and (g) the higher red band (the inner sheet) at $P = 15$ GPa.

states, and a broadening of the $4f$ band as well as a slight decrease of the $4f$ population. One can see a widening of the $4f$ band as well as a clear shift of $4f$ peak to higher energies with pressure, as shown in the inset of Fig. 9.

Figure 10 shows the calculated electronic band structures and Fermi surfaces of $CeAl_2$. There are two bands across the Fermi level, and the corresponding Fermi surfaces are very complex, implying rich physical properties of this material. The group of the bands above the Fermi level is mainly of the Ce-$4f$ character and shifts slightly to higher energies at higher pressure. The near-Fermi bands show a complicated character, including quasiflat bands (e.g., along W-K direction) as well as the bands with higher dispersion $E(k)$ (e.g., along Γ-K, Γ-L directions). The low-lying band (green line) is mainly from Ce d state, whereas the narrow band (red line) is mainly of the Ce f character. By comparing the band structures, an increase of Ce d/f hybridization can be observed along Γ-X and K-Γ directions.

These two bands generate two Fermi surface sheets. The outer sheet contains hole-like sheets on hexagonal lateral faces of the Brillouin zone. The inner sheet exhibits a cage-like structure, due to electron-like sheets. The cage-like structure is connected to other cage-like Fermi surfaces in neighboring Brillouin zones by 6 channels around the X points. On application of pressure the Fermi surfaces change essentially. At $P = 15$ GPa, the cage-like structure is disconnected, and tiny hole pockets appear, which are manifested in the energy band of Fig. 10(e) where the red band crosses the Fermi level four times along K-Γ direction.

IV. CONCLUSIONS

Whether there exists a volume anomaly/discontinuity or not in the intermetallic compound $CeAl_2$ under high pressure has been a long controversy in the past. In order to look for possible anomaly in the compression curve, we have comprehensively studied the acoustic velocities, mechanical properties as well as electronic properties of $CeAl_2$ at high pressure by ultrasonic measurements and first-principles calculations. Anomalous behaviors have been observed in the compressional (V_P) and shear (V_S) wave velocities and elastic moduli in terms of discontinuities and change of slope at around $P = 7.5$ GPa. A volume collapse occurs which might be probably because of a valence transition, showing good agreement with earlier reports. Besides, the pressure-dependent electronic resistance also shows an anomaly at around 7.5 GPa. More interestingly, our DFT calculations predict that the elastic constants C_{11} and C_{44} both show an anomaly at $P = 7.5$ GPa with a change of slope. C_{44} could be the origin of the slow increase of the shear wave velocity and hence the shear modulus observed in our experiments up to 7.5 GPa, since it shows a weak pressure dependence. At higher pressures ($P > 7.5$ GPa), C_{44} softens more rapidly and the shear wave velocity decreases. $CeAl_2$ becomes mechanically unstable for $P > 15$ GPa. Another possible reason for the elastic anomalies might be associated with the softening of TA phonon branches of which the slopes are determined by C_{44}. From the electronic structure calculation, the Ce d/f states hybridization becomes stronger along the high symmetric directions like Γ-X and K-Γ at high pressure, which might be one of the features of the $\gamma - \alpha$ isostructural transition.

ACKNOWLEDGMENTS

This work was supported by National Natural Science Foundation of China (Grant No. 11875238) and Foundation of Science and Technology on Surface Physics and Chemistry Laboratory (Grant No. XKFZ201901). The computational resources utilized in this research were provided by Shanghai Supercomputer Center/Hefei Advanced Computing Center. L. Fang was supported by National Natural Science Foundation of China (Grant No. 12075215). B.L. thanks Dr. Ruizhi Qiu and Dr. Guangxi Jin for helpful discussions on DFT calculations of electronic structure.

[1] G. Y. Guo, Physica B **165–166**, 335 (1990).
[2] F. Lopez-Aguilar and J. Costa-Quintana, Phys. Status Solidi (b) **132**, 485 (1985).
[3] W.-J. Ding, J.-X. Yi, P. Chen, D.-L. Li, L.-M. Peng, and B.-Y. Tang, Solid State Sci. **14**, 555 (2012).
[4] T. Jarlborg, A. J. Freeman, and D. D. Koelling, J. Magn. Magn. Mater. **60**, 291 (1986).
[5] M. Loewenhaupt, W. Reichardt, R. Pynn, and E. Lindley, J. Magn. Magn. Mater. **63–64**, 73 (1987).
[6] P. Thalmeier and P. Fulde, Phys. Rev. Lett. **49**, 1588 (1982).
[7] M. Klicpera, M. Boehm, P. Doležal, H. Mutka, M. M. Koza, S. Rols, D. T. Adroja, I. Puente Orench, J. Rodríguez-Carvajal, and P. Javorský, Phys. Rev. B **95**, 085107 (2017).
[8] D. T. Adroja, A. del Moral, C. de la Fuente, A. Fraile, E. A. Goremychkin, J. W. Taylor, A. D. Hillier, and F. Fernandez-Alonso, Phys. Rev. Lett. **108**, 216402 (2012).
[9] B.-Q. Liu, P. Čermák, C. Franz, C. Pfleiderer, and A. Schneidewind, Phys. Rev. B **98**, 174306 (2018).
[10] P. Čermák, A. Schneidewind, B. Liu, M. M. Koza, C. Franz, R. Schönmann, O. Sobolev, and C. Pfleiderer, Proc. Natl. Acad. Sci. USA **116**, 6695 (2019).
[11] B. Barbara, J. Y. Boucherle, J. L. Buevoz, M. F. Rossignol, and J. Schweitzer, Solid State Commun. **24**, 481 (1977).
[12] S. M. Shapiro, E. Gurewitz, R. D. Parks, and L. C. Kupferberg, Phys. Rev. Lett. **43**, 1748 (1979).
[13] E. M. Forgan, B. D. Rainford, S. L. Lee, J. S. Abell, and Y. Bi, J. Phys.: Condens. Matter **2**, 10211 (1990).
[14] M. Nicolas-Francillon, A. Percheron, J. C. Achard, O. Gorochov, B. Comut, D. Jerome, and B. Coqblin, Solid State Commun. **11**, 845 (1972).
[15] G. Oomi, M. Ohashi, Y. Uwatoko, I. Satoh, and T. Komatsubara, Phys. B: Condens. Matter **359-361**, 65 (2005).
[16] H. Miyagawa, M. Ohashi, G. Oomi, I. Satoh, and T. Komatsubara, Phys. B: Condens. Matter **378-380**, 771 (2006).
[17] T. Sawamura, T. Andoh, G. Oomi, and Y. Onuki, Rev. High Pressure Sci. Technol. **7**, 614 (1998).
[18] C. Probst and J. Wittig, J. Magn. Magn. Mater. **9**, 62 (1978).

[19] H. Miyagawa, G. Oomi, M. Ohashi, I. Satoh, T. Komatsubara, M. Hedo, and Y. Uwatoko, Phys. Rev. B **78**, 064403 (2008).

[20] H. Miyagawa, M. Ohashi, T. Nakano, G. Oomi, I. Satoh, and T. Komatsubara, J. Phys.: Conf. Ser. **150**, 042127 (2009).

[21] E. Hanke and A. Eichler, High Pressure Res. **3**, 180 (1990).

[22] A. Eichler, E. Hanke, and J. Michal, Phys. B: Condens. Matter **194-196**, 183 (1994).

[23] M. Kontani, N. Sugihara, K. Murase, and N. Môri, Czech. J. Phys. **46**, 2067 (1996).

[24] M. Croft and A. Jayaraman, Solid State Commun. **29**, 9 (1979).

[25] M. Croft and A. Jayaraman, Solid State Commun. **35**, 203 (1980).

[26] H. Bartholin, A. Waintal, G. Parisot, F. Kervella, and J. P. Senateur, Phys. Status Solidi (a) **61**, K87 (1980).

[27] T. G. Ramesh, A. S. Reshamnala, and S. Ramaseshan, Solid State Commun. **15**, 1851 (1974).

[28] V. Vijayakumar, S. N. Vaidya, E. VB. Sampathkumaran, and R. Vijayaraghavan, Solid State Commun. **46**, 549 (1983).

[29] T. G. Ramesh and W. B. Holzapfel, Pramana–J. Phys. **29**, 183 (1987).

[30] B. Barbara, J. Beille, B. Cheiato, J. M. Laurant, M. F. Rossignol, A. Waintal, and S. Zemirli, Phys. Lett. A **113**, 381 (1986).

[31] B. Barbara, J. Beille, B. Cheaito, J. M. Laurant, M. F. Rossignol, A. Waintal, and S. Zemirli, J. Phys. France **48**, 635 (1987).

[32] I. Vedel, A. M. Redon, J. M. Léger, J. M. Mignot, and J. Flouquet, J. Magn. Magn. Mater. **54-57**, 361 (1986).

[33] I. Vedel, A.-M. Redon, J.-M. Mignot, and J.-M. Leger, J. Phys. F: Met. Phys. **17**, 849 (1987).

[34] N. V. Chandra Shekar, P. Ch. Sahu, M. Yousuf, K. Govinda Rajan, M. Rajagopalan, Solid State Commun. **111**, 529 (1999).

[35] S. Tateno, N. Kishii, M. Ohashi, H. Miyagawa, G. Oomi, I. Satoh, N. Miyajima, and T. Yagi, J. Phys.: Conf. Ser. **950**, 042030 (2017).

[36] B. Li and R. C. Liebermann, Phys. Earth Planet. Inter. **233**, 135 (2014).

[37] G. Kresse and J. Hafner, Phys. Rev. B. **47**, 558 (1993).

[38] G. Kresse and J. Furthmüller, Phys. Rev. B **54**, 11169 (1996).

[39] R. K. Cook, J. Acoust. Soc. Am. **29**, 445 (1957).

[40] W. Liu, Q. S. Zeng, Q. K. Jiang, L. P. Wang, and B. S. Li, Scr. Mater. **65**, 497 (2011).

[41] D. Schreiber, *Elastic Constants and Their Measurement* (McGraw-Hill, New York, 1973).

[42] G. Davies and A. Dziewonski, Phys. Earth Planet. Inter. **10**, 336 (1975).

[43] C. Probst and J. Wittig, in *Handbook on the Physics and Chemistry of Rare Earths*, edited by K. A. Gschneidner Jr. and L. Eyring (North-Holland, Amsterdam, 1978), Vol. 1, pp. 749–795.

[44] H. H. Hill, in *Plutonium 1970 and Other Actinides*, edited by W. N. Miner (Aime, New York, 1970), p. 2.

[45] T. Penny, B. Barbara, T. S. Plaskett, H. E. King, Jr., and S. J. LaPlaca, Solid State Commun. **44**, 1199 (1982).

[46] F. Birch, Phys. Rev. **71**, 809 (1947).

[47] V. Raghavan, J. Phase Equilib. **28**, 189 (2007).

[48] B. Apparao, P. Kistaiath, N. Raja Shekhar Reddy, and K. Satyanarayna Murthy, J. Less-Common Metals **95**, 93 (1983).

[49] M. F. Rossignol, Thése de Doctorat d'Etat, University of Gernoble, 1980.

[50] B.-Q. Liu, L. Xie, X.-X. Duan, G.-A. Sun, B. Chen, J.-M. Song, Y.-G. Liu, and X.-L. Wang, Acta Phys. Sin. **62**, 176104 (2013).

[51] B.-Q. Liu, X.-X. Duan, G.-A. Sun, J.-W. Yang, and T. Gao, Phys. Chem. Chem. Phys. **17**, 4089 (2015).

[52] Y. S. Cheng and B. Q. Liu, J. Sichuan Univ: Nat. Sci. Ed. **58**, 054005 (2021).

[53] X. Qi, X. Wang, T. Chen, and B. Li, J. Appl. Phys. **119**, 125109 (2016).

[54] F. Mouhat and F. X. Coudert, Phys. Rev. B. **90**, 224104 (2014).

[55] W. Reichardt and N. Nücker, J. Phys. F: Met. Phys. **14**, L135 (1984).

[56] M. Godet and H.-G. Purwins, Solid State Commun. **21**, 761 (1977).

[57] S. Roth, A. Wurzinger, and H.-G. Purwins, Phys. Lett. A **72**, 242 (1979).

[58] B. Lüthi and C. Lingner, Z. Phys. B **34**, 157 (1979).

[59] R. Hill, Proc. Phys. Soc. **65**, 349 (1952).

[60] S. F. Pugh, Philos Mag. **45**, 823 (1954).

[61] F. López-Aguilar and J. Costa-Quintana, Phys. Status Solidi (b) **138**, 589 (1986).